

Relic density of dark matter in the inert doublet model beyond leading order for the low mass region: 3. Annihilation in 3-body final state

Shankha Banerjee^a, Fawzi Boudjema^b, Nabarun Chakrabarty^{c,d}, Hao Sun^e

^a*CERN, Theoretical Physics Department, CH-1211 Geneva 23, Switzerland*

^b*LAPTh, Université Savoie Mont Blanc, CNRS, BP 110, F-74941 Annecy-le-Vieux, France*

^c*Centre for High Energy Physics, Indian Institute of Science, C.V. Raman Avenue, Bangalore 560012, India*

^d*Department of Physics, Indian Institute of Technology Kanpur, Kanpur, Uttar Pradesh 208016, India*

^e*Institute of Theoretical Physics, School of Physics, Dalian University of Technology, Dalian 116024, People's Republic of China*

E-mail: shankha.banerjee@cern.ch, boudjema@lapth.cnrs.fr,
chakrabartynabarun@gmail.com, haosun@dlut.edu.cn

ABSTRACT: We perform the first one-loop electroweak corrections for $2 \rightarrow 3$ processes for dark matter annihilation. These are the dominant processes that enter the computation of the relic density for the low mass region of the inert doublet model (IDM) when annihilations to two on-shell vector bosons are closed. The impact of the one-loop corrections are important as they involve, through rescattering effects, not only a dependence on the parameter controlling the dark sector, not present if a calculation at tree-level is conducted, but also on the renormalisation scale. These combined effects should be taken into account in analyses based on tree-level cross-sections of the relic density calculations, as a theoretical uncertainty which we find to be much larger than the cursory $\pm 10\%$ uncertainty that is routinely assumed, independently of the model parameters.

1 Introduction

The fermions of the the standard model (SM) do not directly couple to the scalars in the inert doublet model (IDM) [1–47]. The annihilation of the dark matter (DM) candidate in the IDM, the lightest neutral scalar X , occurs most naturally through annihilation into the SM vector bosons. These processes are triggered by the gauge coupling and also by the interactions stemming from the scalar sector of the model. The latter can be parametrised by the coupling of the SM Higgs to the pair of DM, λ_L , once the masses of all the scalars of the IDM are derived [48]. For these annihilations into a pair of WW and ZZ to be possible, the mass of the DM, M_X , must be larger than M_W , the mass of the W -boson. Even in this case, these annihilations are so efficient, see [48], that the obtained relic density is too small, unless one considers very high DM masses [49]. For the low mass, $M_X < M_W$, DM region of the IDM [48], the annihilations are into WW^* and ZZ^* where one of the vector bosons is off-shell and is materialised by a fermion pair. The cross-sections are then smaller, bringing the relic density in accord with present measurement of the relic density. For WW^* and ZZ^* , one is then faced with the calculation of a $2 \rightarrow 3$ process which has never been attempted at one-loop for the calculation of the relic density. Unlike the newly discovered co-annihilation region and the Higgs resonance region, this continuum region does not require much adjustment of the parameters in order to achieve a good value of the relic density within the freeze-out mechanism. This explains why a scan on the parameters of the IDM returns quite a few points with this topology for the relic density. Following the in-depth preliminary study, $XX \rightarrow W^+W^-, ZZ$, of all the possible benchmarks in this region that pass all the experimental (and theoretical) constraints, we retain, in the present analysis of these channels, only those benchmarks which satisfy the one-loop perturbativity requirement [48]. This requirement was enunciated in the preparatory study $XX \rightarrow W^+W^-, ZZ$ [48]. In a nutshell, only models that return small enough $\tilde{\beta}_{\lambda_L}$ (the β -function parameter that controls the running of the coupling λ_L) are perturbative [48]. On that basis, we keep three benchmark points defined in [48]: (points A, F and G) to illustrate our computations of the one-loop electroweak corrections to $XX \rightarrow Zf\bar{f}$ and $XX \rightarrow Wf\bar{f}'$. Let us therefore recall the characteristics of these three benchmark points in Table 1.

	A	F	G
M_X	70	72	72
$\lambda_L \times 10^3$	5.0	3.8	0.1
M_A, M_{H^\pm}	170,200	138,138	158,158
$(\lambda_3, \lambda_4, \lambda_5)$	(1.127, -0.738, -0.384)	(0.447, -0.222, -0.222)	(0.632, -0.316, -0.316)
$\tilde{\beta}_{\lambda_L}$	$4.343 + 6.082\lambda_2$	$1.402 + 2.704\lambda_2$	$2.142 + 3.795\lambda_2$
Ωh^2			
$\alpha(0)$	0.156	0.119	0.121
$\Omega_{WW^*}(\%)$	90	88	88
$\Omega_{ZZ^*}(\%)$	10	12	12

Table 1: Characteristics of the benchmark points A, F and G. All masses are in GeV. The tree-level (calculated with $\alpha(0)$) relic density and the weight in percent of each channel contributing to the relic density, are given. We also list the values of the underlying parameters $\lambda_{3,4,5}$ and $\tilde{\beta}_{\lambda_L}$ [48].

The paper is organised as follows. In the next section, we review the $2 \rightarrow 3$ cross-sections and seek a factorisation where the flavour dependence is carried by the vector bosons' partial widths. Section 3 is a general presentation of the one-loop calculation. Since the bulk of the corrections are contained in the purely virtual correction in the neutral channel $Z\nu\bar{\nu}$, section 4 is dedicated to this channel before studying in section 5 all the other channels where final state radiation (tree-level $2 \rightarrow 4$ processes are

needed) is considered. Section 6 summarises all the one-loop results on the cross-sections leading the way to the impact of the corrections and the scale uncertainty on the relic density which we present in section 7. Our conclusions are presented in section 8.

2 Tree-level considerations

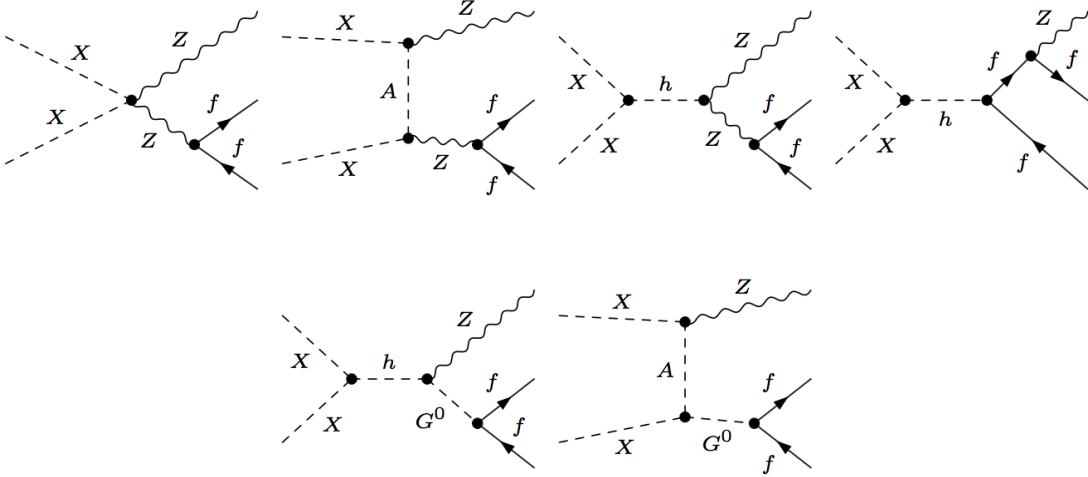


Figure 1: A selection of tree-level Feynman diagrams for $XX \rightarrow Zf\bar{f}$ in the Feynman gauge. The displayed diagrams can be built up from $XX \rightarrow ZZ^* \rightarrow Zf\bar{f}$ but note also the Z -“bremsstrahlung” contribution triggered from $XX \rightarrow ff^* \rightarrow f\bar{f}Z$ (last diagram in the first row).

Like for the $2 \rightarrow 2$ processes, $XX \rightarrow WW$ and $XX \rightarrow ZZ$, beside the masses of the dark sector particles, the cross-sections depend not only on the gauge coupling but also on λ_L (because of the SM Higgs exchange and the quartic $XXVV$ couplings, $V = W, Z$). The massive fermions’ Yukawa couplings may also play a role, but we will see that they are negligible. As a subset, contributions to the full $Zf\bar{f}$ is displayed in Figure 1.

It is completely unwise to try to compute such cross-sections, even at tree-level, by splitting them into a $2 \rightarrow 2$ process followed by the “decay” of one of the vector bosons into fermions even if the Z/W current is conserved in the limit $m_f \rightarrow 0$. For starters, $XX \rightarrow VV^*$ is ill-defined since it does not correspond to an element of the S -matrix. Therefore, a complete $2 \rightarrow 3$, $XX \rightarrow Zf\bar{f}$ and $XX \rightarrow Wf\bar{f}'$, calculation is in order. Nonetheless, because the mass of the final fermions is very small compared to the energies involved and the fact that the fermions do not couple to the dark sector, we expect that the complete calculation of the cross-sections are arranged such that

$$\frac{\sigma(XX \rightarrow Zf\bar{f})}{\sigma(XX \rightarrow Z\nu\bar{\nu})} \simeq \frac{\Gamma_{Z \rightarrow f\bar{f}}}{\Gamma_{Z \rightarrow \nu\bar{\nu}}} = \frac{\text{Br}_{Z \rightarrow f\bar{f}}}{\text{Br}_{Z \rightarrow \nu\bar{\nu}}}, \quad (2.1)$$

$$\frac{\sigma(XX \rightarrow Wf\bar{f}')}{\sigma(XX \rightarrow W\nu_e\bar{e})} \simeq \frac{\Gamma_{W \rightarrow f\bar{f}'}}{\Gamma_{W \rightarrow \nu_e\bar{e}}} \simeq N_c^f, \quad (N_c^f = 1, 3 \text{ is the colour factor}). \quad (2.2)$$

The ratios of the partial physical widths act as a normalisation of the cross-sections with respect to

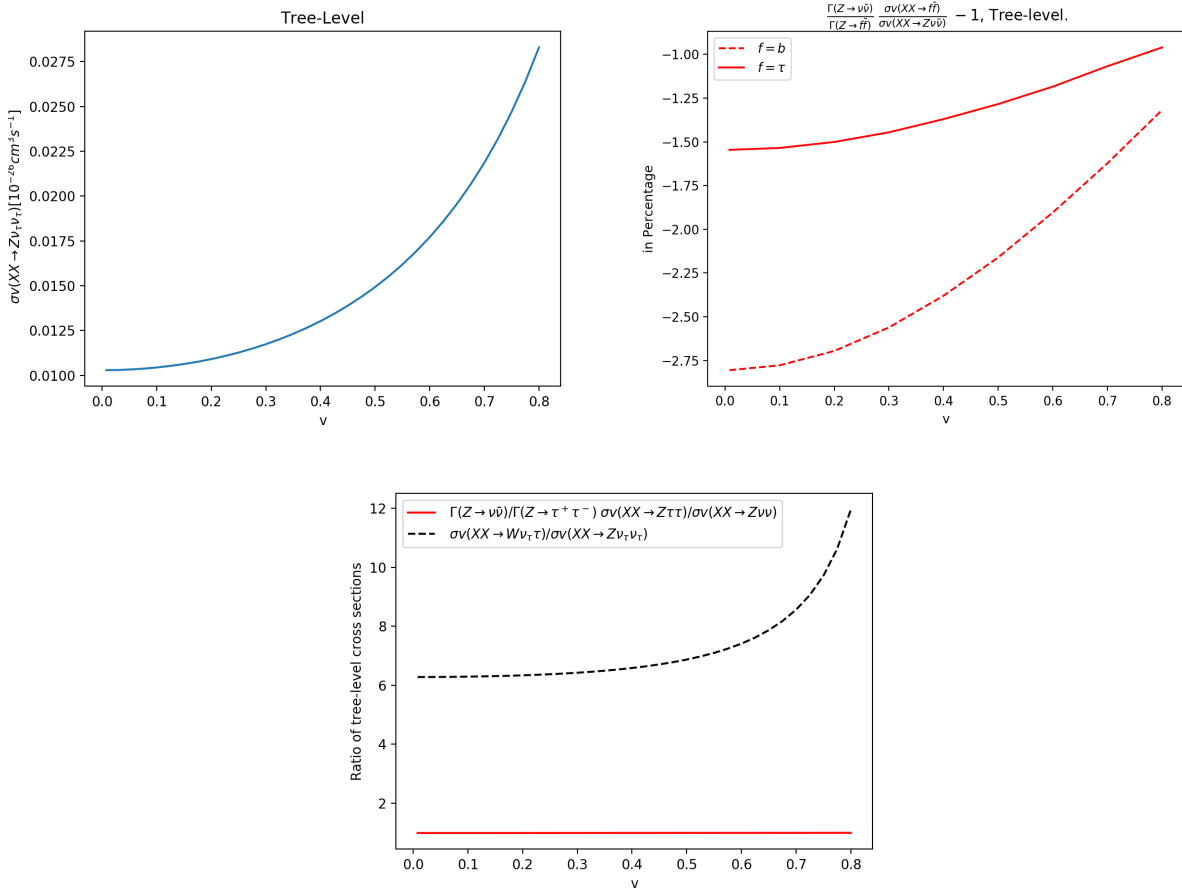


Figure 2: *Benchmark Point G.* The tree-level cross-section times the relative velocity for $XX \rightarrow Z\nu\bar{\nu}$ (upper-left panel), $R_{Zf\bar{f}}^{XX} - 1$ for $f = \tau, b$ (upper-right panel). The lower panel displays $R_{Z\tau\bar{\tau}}^{XX} \simeq 1$ and the ratio of the tree-level cross-sections $R_{W/Z}^{XX} = \sigma(XX \rightarrow W\tau\bar{\nu}_\tau)/\sigma(XX \rightarrow Z\nu_\tau\bar{\nu}_\tau)$ as a function of the relative velocity, v .

the neutrino channels. If we introduce

$$\begin{aligned}
 R_{Zf\bar{f}}^{XX} &= \frac{\sigma(XX \rightarrow Zf\bar{f})}{\sigma(XX \rightarrow Z\nu\bar{\nu})} \frac{\Gamma_{Z \rightarrow \nu\bar{\nu}}}{\Gamma_{Z \rightarrow f\bar{f}}} \\
 R_{Wf\bar{f}'}^{XX} &= \frac{\sigma(XX \rightarrow Wf\bar{f}')}{\sigma(XX \rightarrow W\nu_e\bar{e})} \frac{\Gamma_{W \rightarrow \nu_e\bar{e}}}{\Gamma_{W \rightarrow f\bar{f}'}} \\
 R_{W/Z}^{XX} &= \frac{\sigma(XX \rightarrow W\nu_e\bar{e})}{\sigma(XX \rightarrow Z\nu\bar{\nu})}, \tag{2.3}
 \end{aligned}$$

it follows from the arguments that lead to Equations 2.1- 2.2 that $R_{Zf\bar{f}}^{XX} \sim R_{Wf\bar{f}'}^{XX} \sim 1$. We verify these approximations and behaviour by carrying a full calculation with fermion mass effect for the different channels. For Point G, the results are displayed in Figure 2.

First of all, the velocity dependence of the tree-level $XX \rightarrow Zf\bar{f}$ and $XX \rightarrow Wf\bar{f}'$ is strong. This is shown in Figure 2 for the $Z\nu\bar{\nu}$ and consequently for $W\bar{\nu}_\tau\tau$. The latter grows faster past $v \sim 0.5$. This is understandable since as v increases one gets closer to the opening of the threshold for on-shell pair production of vector bosons, the WW threshold occurring first. The important observation though is that below $v \sim 0.5$ (the most important range for the relic density calculation), when the threshold effect is small, the ratio between these two cross-sections is almost constant. This is due to the global $SU(2)$ symmetry with the important consequence that the λ_L dependence is the same in the

neutral and charged channels. This is the same property that is explicitly confirmed in $XX \rightarrow WW$ and $XX \rightarrow ZZ$ past the ZZ threshold in our study in Ref. [48]. The same λ_L dependence will mean that both channels will exhibit the same scale uncertainty in the one-loop corrected cross-sections.

We confirm this feature at all v , and independently of the flavour $R_{Wf\bar{f}'}^{XX} = 1$, at better than the per-mille level, to the point where we can not display this difference in Figure 2.

In the neutral channel, $R_{Zf\bar{f}}^{XX} \simeq 1$ is also nicely confirmed. Departure from unity are largest for the $Zb\bar{b}$ final state where the maximal value is below 3% across all values of v . The effect is smaller still for the $Z\tau\tau$ channel as seen in Figure 2. For all other channels, the mass effects are unnoticeable and are therefore not shown in the figure. The effect of the fermion masses/Yukawa couplings through Higgs exchange, $XX \xrightarrow{h} ff^* \rightarrow f\bar{f}Z$, is therefore small.

Taken together, these observations lead us to conclude that the cross-section into the neutrinos can be taken as a representative of the channels, neutral and charged. We also look at $R_{W/Z}^{XX}$. For the moment we keep these observations in mind before attempting the one-loop analyses. This first exploration confirms that the neutrino channels carry the bulk of the v dependence and are the prime channels against which we will measure all other channels. We also confirm that the same conclusions, with the same level of accuracy, apply for the other benchmark points (A and F).

3 $XX \rightarrow Wf\bar{f}'$ and $XX \rightarrow Zf\bar{f}$ at one-loop: General issues

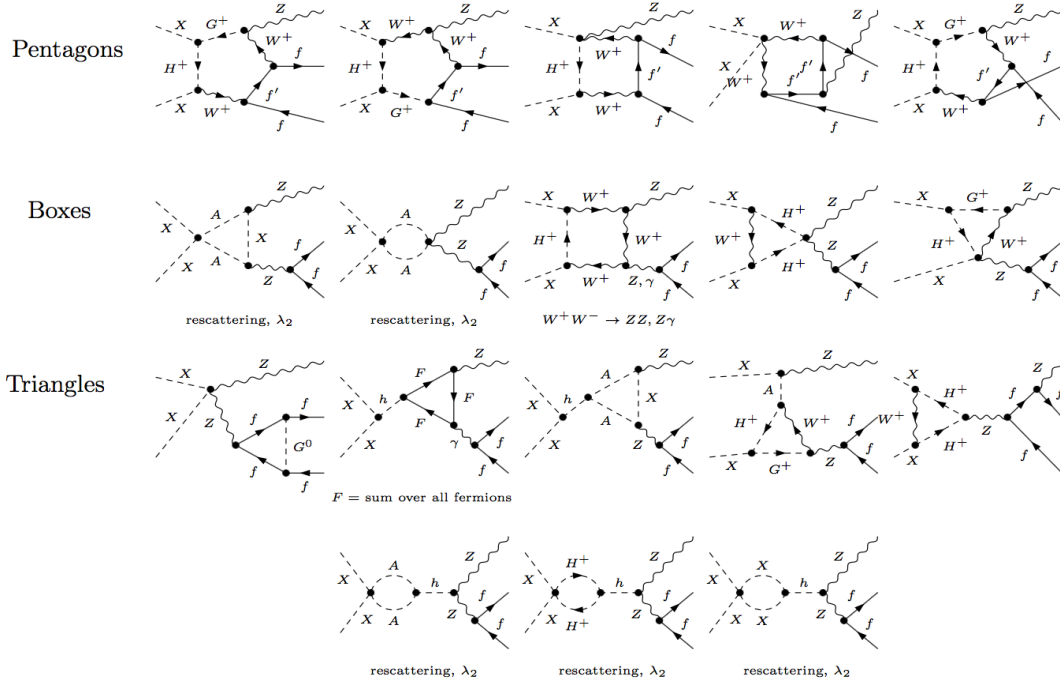


Figure 3: A small selection of Feynman diagrams for $XX \rightarrow Zf\bar{f}$ at one-loop. We only show a very small subset of pentagons, boxes and triangles but not self-energy corrections and counterterms. f' stands for the $SU(2)$ partner of f (ν_l for $f = l$). F stands for the sum of all SM fermions. Although some diagrams may not look like boxes, they fall under the box category because of the 4-particle vertices they involve. The same applies to triangles. We see rescattering effects within the dark sector, $XX \rightarrow AA, H^+H^-, XX$ that explicitly involve the λ_2 parameter that does not show up at tree-level. Note also that because of the off-shell Z , charged fermions ff pairs from γ^* must also be taken into account.

At one-loop, a large number of topologies appears for these $2 \rightarrow 3$ processes. For $XX \rightarrow Zf\bar{f}$, a set of the contributing one-loop diagrams is shown in Figure 3. A subset of diagrams at one-loop for $XX \rightarrow Wf\bar{f}$ is found in our analysis of the co-annihilation region where this cross-section was a subdominant contribution to the relic density [50]. Technically, it is not (only) the sheer number of diagrams that adds to the complexity of the calculation but also the fact that the calculation, especially the reduction of the n -point integrals, is very much computer-time consuming. This is particularly the case for the 5-point functions, the pentagons, that need to be evaluated, for instance, in configurations of phase space where $v \sim 0$, dangerously close to the appearance of very small Gram determinants, see [51]. For the charged final state, tree-level $XX \rightarrow Zf\bar{f}\gamma$ and $XX \rightarrow Wf\bar{f}\gamma$ must be considered together with the virtual one-loop corrections. We find that the phase space slicing method, as applied in [49], converges relatively quickly. Gauge parameter independence [48] is carried at some random point in phase space. This is a check not only on the model implementation (including counterterms) but also the tensorial reduction of the loop integrals.

An on-shell scheme for λ_L based on $h \rightarrow XX$ is not possible for this mass range since this decay is closed. The radiative correction will therefore be sensitive to the renormalisation scale, μ , associated with the $\overline{\text{MS}}$ scheme associated with a definition of λ_L , see [48],

$$\delta^{\overline{\text{MS}}}\lambda_L = \frac{1}{32\pi^2}\tilde{\beta}_{\lambda_L}C_{UV}, \quad C_{UV} = -\frac{2}{\varepsilon} - 1 + \gamma_E - \ln(4\pi), \quad (3.1)$$

where $\varepsilon = 4 - d$ with d being the number of dimensions in dimensional regularisation and γ_E being the Euler-Mascheroni constant. With μ_{dim} , the scale introduced by dimensional regularisation, the scale, Q^2 , dependence of λ_L is

$$32\pi^2 \frac{\partial \lambda_L}{\partial \ln(Q^2)} = -32\pi^2 \frac{\partial \lambda_L}{\partial \ln(\mu_{\text{dim}}^2)} = \tilde{\beta}_{\lambda_L}. \quad (3.2)$$

We will, for the three benchmark points in this mass range, study the scale dependence. Beside the scale dependence, we also investigate the interesting λ_2 dependence which, as we showed in $XX \rightarrow WW, ZZ$ above threshold, is not totally contained in β_{λ_L} , see [48]. The scale dependence, for a fixed v , is easily extracted from the λ_L dependence of the tree-level cross-section combined with the expression of β_{λ_L} which is known analytically. Barring very small mass effects, we confirm that at tree-level $R_{Zf\bar{f}}^{XX} \simeq 1$, $R_{Wf\bar{f}'}^{XX} = 1$, while $R_{W/Z}^{XX}$ has a slight v dependence above $v > 0.5$. This is an indication that the λ_L dependence of the cross-section is essentially the same for all fermion channels in $XX \rightarrow Zf\bar{f}$ and $XX \rightarrow Wf\bar{f}'$.

Before displaying the numerical results of the full one-loop computation, we present the analytical scale variation for a chosen relative velocity in order to weigh how strong the scale dependence can be. From what we argued and will confirm shortly through a full calculation, the bulk of the scale variation is almost flavour independent. We therefore first concentrate on the neutral channel $XX \rightarrow Z\nu\bar{\nu}$. The most important features that are present in all other channels, are revealed in this channel. From the computation point of view, the neutrino channel is somehow the easiest since we do not need to deal with the infrared singularities that require the inclusion of the radiative $2 \rightarrow 4(3 + \gamma)$ tree-level contribution.

4 $XX \rightarrow ZZ^*$ at one-loop: $XX \rightarrow Z\nu\bar{\nu}$

The large number of diagrams and the appearance of 5-point function loop integrals makes these computations challenging but SloopS [49, 51–58], our automated code, has been optimised to deal with many of the technicalities that are involved in these calculations. Another sort of technicality

is the renormalisation and in particular the scheme dependence. All parameters but, in this case, λ_L are defined on-shell. λ_L is here taken $\overline{\text{MS}}$, and at the end the one-loop result carries a scale dependence. As shown in details in the accompanying paper [48], the scale dependence in this mixed scheme only originates from the λ_L counterterm. One can even exactly determine the scale dependence of the one-loop cross-section from the parametric λ_L dependence of the tree-level cross-section and the knowledge of the corresponding β function for λ_L , $\tilde{\beta}_{\lambda_L}$, which can be derived analytically. That such an approach agrees with the result of a direct calculation for an arduous calculation such as this $2 \rightarrow 3$ process, is a further strong indication of the correctness of the calculation beside the tests of ultra-violet (UV) finiteness and gauge parameter independence. Moreover, such an approach which allows an analytical parametrisation of the scale, is very useful. The first step is to seek the λ_L parametric dependence of the tree-level cross-section at a given v . To extract this, we maintain all parameters of the model, namely the masses and the SM parameters fixed apart from λ_L . Since the dependence is a quadratic polynomial, the λ_L dependence is reconstructed numerically by generating the cross-sections for $\lambda_L = 0, 1, 2$. We check the goodness of the parameterisation by taking a random value of λ_L and comparing the cross-section obtained from the reconstructed polynomial against a direct calculation using the code. We always find excellent agreement for this check. One can then derive the infinitesimal change of the cross-section due to an infinitesimal change of λ_L . The latter will then be turned to a change due to the counterterm for λ_L through $\tilde{\beta}_{\lambda_L}$ which quantifies the scale dependence as we will see next for our three benchmark points.

4.1 $XX \rightarrow Z\nu\bar{\nu}$ at Point G

The λ_L dependence of the cross-section, for $v = 0.4$, is found to be

$$\sigma_{XX \rightarrow Z\nu\bar{\nu}, G}^0(v = 0.4) v = 0.013 + 0.300\lambda_L + 1.750\lambda_L^2 \simeq 0.013(1 + 23\lambda_L + 135\lambda_L^2). \quad (4.1)$$

Observe that the λ_L dependence is quite strong. The (relative) coefficient of λ_L is about 23. Note also that the λ_L^2 is even larger. The latter will not be so important since the constraints posed on λ_L give very small values of λ_L . One can then relate the one-loop correction $d\sigma(\mu_2)$ at scale μ_2 to the one at scale μ_1 according to

$$\begin{aligned} d\sigma_{XX \rightarrow Z\nu\bar{\nu}}^{G, v=0.4}(\mu_2) v &= d\sigma_{XX \rightarrow Z\nu\bar{\nu}}^{G, v=0.4}(\mu_1) v - \left(0.300 + 2 \times 1.750\lambda_L\right) \frac{\beta_{\lambda_L} \ln(\mu_2/\mu_1)}{16\pi^2}, \\ &\sim d\sigma_{XX \rightarrow Z\nu\bar{\nu}}^{I, v=0.4}(\mu_1) v - 0.300 \left(2.141 + 3.795\lambda_2\right) \frac{\ln(\mu_2/\mu_1)}{16\pi^2}, \quad \text{leading to} \\ \left. \frac{d\sigma_{XX \rightarrow Z\nu\bar{\nu}}(2\mu_1)}{\sigma_{XX \rightarrow Z\nu\bar{\nu}}^0} \right|_{G, v=0.4} &\sim \left(\left. \frac{d\sigma_{XX \rightarrow Z\nu\bar{\nu}}(\mu_1)}{\sigma_{XX \rightarrow Z\nu\bar{\nu}}^0} \right|_{I, v=0.4} - 21.7 (1 + 1.8\lambda_2) \right) \%. \end{aligned} \quad (4.2)$$

The last line gives the difference when the scale is doubled from μ_1 to $2\mu_1$.

We verify these formulae against the results of a direct computation of the full one-loop correction. We obtain a 5 digit agreement for three values of λ_2 ($\lambda_2 = 0.01, 1, 2$) and different combinations of the scale μ . We note that the scale dependence is quite large. This is due to the strong λ_L dependence of the cross-section and also to the fact that $\tilde{\beta}_{\lambda_L}$ is not so small. For this benchmark point and for $v = 0.4$ we learn from Equation 4.2 that, in the range $M_X/2 < \mu < 2M_X$, the uncertainty introduced by the scale variation is about 44% for $\lambda_2 = 0$, it increases to about 200% for $\lambda_2 = 2$, which should be quoted as the overall theoretical uncertainty if we allow both the scale μ to span the range $M_X/2 - 2M_X$ and a variation $0 < \lambda_2 < 2$.

The results of the full one-loop corrections for three values of $\lambda_2 = 0.01, 1, 2$ and for different scales, $\mu = M_X/2, M_X, 2M_X$ are displayed in Figure 4 for the range of relative velocities of interest

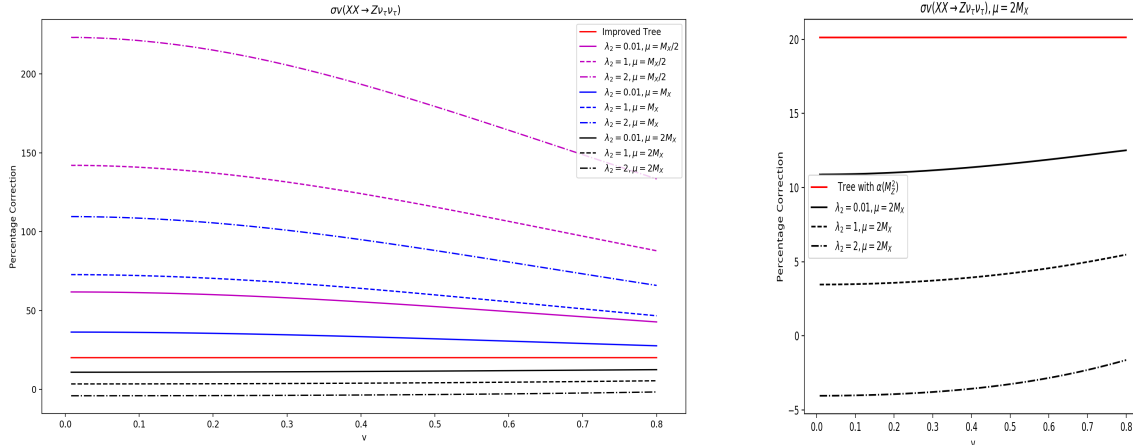


Figure 4: Point G. Comparing the relative correction in % as a function of the relative velocity for $Z\nu_\tau\bar{\nu}_\tau$ for $\lambda_2 = 0.01, 1, 2$ and for 3 scales $\mu = M_X/2, M_X, 2M_X$. We also display the improved tree-level based on the use of $\alpha(M_Z^2)$. The panel on the right is a zoom on the choice $\mu = 2M_X$ for better readability.

for the relic density calculation. The so-called improved tree-level based on the use of $\alpha(M_Z^2)$ gives a constant correction of about 21%. $\mu = M_X/2$ gives not only the largest correction but shows also a significant velocity dependence. $\mu = M_X/2$ is not an appropriate scale, this scale is quite removed from the (largest) scales that enter the loop integrals: the invariant mass of the XX system $\sqrt{s_{XX}} \simeq 2M_X(1 + v^2/8) \sim 2M_X$ or M_A that enter in the t -channel exchange. As discussed in [48], the appropriate scale should be, $\max(2M_X, M_A) = 158$ GeV. For point G, there is a small difference of 14 GeV between $2M_X$ and M_A . We will come back to the choice $\mu = M_A$ whose results will be close to what we obtain for $2M_X$. Our results show that for $\mu = 2M_X$ and $\lambda_2 = 0.01$, the correction is about 11%. It decreases slowly as λ_2 increases. With this choice of the scale, the corrections range from 11% to -3% for λ_2 ranging from 0.01 to 2. Observe that while for $\lambda_2 = 0.01$ the corrections are closest to the value obtained with the *improved tree-level* cross-section ($\alpha(M_Z^2)$), there is still as much as 10% difference between the two corrections. An important lesson is that the λ_2 dependence of the full one-loop correction is clearly important. This λ_2 dependence is not all contained in $\tilde{\beta}_{\lambda_L}$.

4.2 $XX \rightarrow Z\nu\bar{\nu}$ at Points F and A

Benchmark points A and F show similar trends to what we just saw for Point G despite the fact that both benchmarks points A and F have a much larger value of λ_L . This is understandable since the crucial property that explains the scale dependence is on the one-hand the relative λ_L dependence on the cross-section and on the other the value of $\tilde{\beta}_{\lambda_L}$ and its λ_2 dependence. The λ_L dependence of the tree-level cross-section is not very different from that of point G. What is quite different is the magnitude of β_L and its λ_2 dependence. Point F (A) has a smaller (larger) β_L (about a factor 2 for the same value of λ_2) than Point G. When selecting the most appropriate scale we observe that for point A, M_A is the most appropriate scale while for point F, $2M_X$ is quite close to M_A .

From the λ_L dependence of the tree-level cross-section of point F, at $v = 0.4$, we have

$$\sigma_{XX \rightarrow Z\nu\bar{\nu}, F}^0(v = 0.4) \simeq 0.012 (1 + 24\lambda_L + 143\lambda_L^2), \quad (4.3)$$

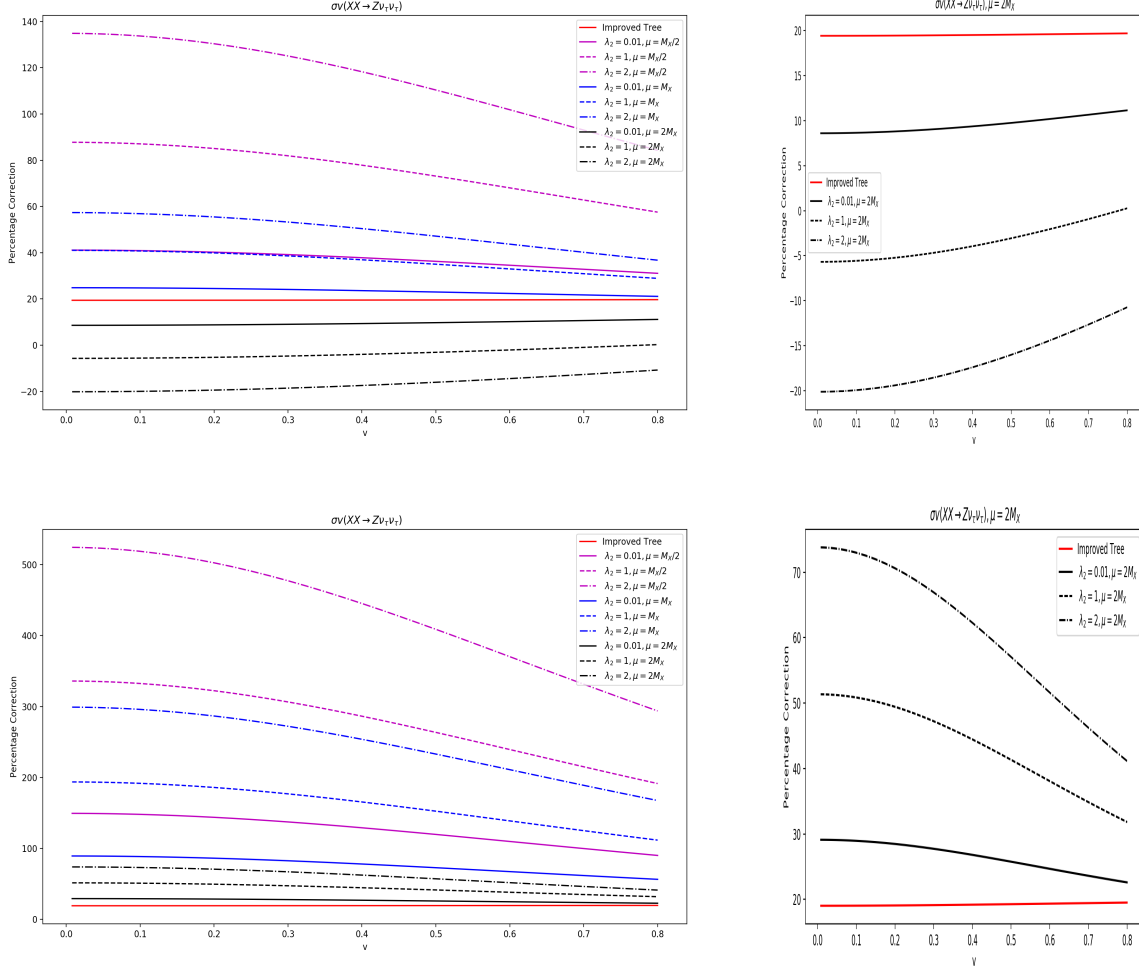


Figure 5: As in 4 but for Point F (upper panels) and Point A (lower panels).

so that the percentage correction is

$$\frac{d\sigma_{XX \rightarrow Z\nu\bar{\nu}}(\mu_2)}{\sigma_{XX \rightarrow Z\nu\bar{\nu}}^0} \Big|_{F,v=0.4} \simeq \left(\frac{d\sigma_{XX \rightarrow Z\nu\bar{\nu}}(\mu_1)}{\sigma_{XX \rightarrow Z\nu\bar{\nu}}^0} \Big|_{F,v=0.4} - 20.1 (1 + 1.9\lambda_2) \ln(\mu_2/\mu_1) \right) \% \quad (4.4)$$

while for point A, we have

$$\sigma_{XX \rightarrow Z\nu\bar{\nu},A}^0(v = 0.4) v \simeq 0.009 (1 + 28\lambda_L + 201\lambda_L^2), \quad (4.5)$$

giving

$$\frac{d\sigma_{XX \rightarrow Z\nu\bar{\nu}}(\mu_2)}{\sigma_{XX \rightarrow Z\nu\bar{\nu}}^0} \Big|_{A,v=0.4} \simeq \left(\frac{d\sigma_{XX \rightarrow Z\nu\bar{\nu}}(\mu_1)}{\sigma_{XX \rightarrow Z\nu\bar{\nu}}^0} \Big|_{A,v=0.4} - 72.1 (1 + 1.4\lambda_2) \ln(\mu_2/\mu_1) \right) \% \quad (4.6)$$

Our results for points F and A are shown in Figure 5. They confirm the general trend observed for point G. The full one-loop results displaying the scale dependence and λ_2 dependence are also in excellent agreement with the analytical formulae of Equations 4.4-4.6. For $\mu = M_X/2$, the corrections are very large with strong velocity dependence. Of the three scales, $\mu = M_X/2, M_X, 2M_X$, the largest scale, $\mu = 2M_X$, is where the corrections are the smallest. Yet, for point A, even $\mu = 2M_X$ gives large correction. For point A, M_A is the largest scale for the process. It is quite different from the choice

$\mu = 2M_X$, considering the large value of $\tilde{\beta}_{\lambda_L}$. We therefore show the results of taking $\mu = M_A$ as the optimised scale in Figure 6. For Point F, the difference with $\mu = 2M_X$ is very small and changes (slightly) mainly the results for $\lambda_2 = 2$ (there is an upward shift of -5% when moving from $\mu = 2M_X$ to $\mu = M_A$). This is due to the fact that for point F, $2M_X$ and M_A are very close ($M_A = 138$ GeV and $2M_X = 144$ GeV) and $\tilde{\beta}_{\lambda_L}$ is not large. The effect of the change of μ for point A when moving between the scale $2M_X$ and M_A is substantial. In particular, for $\lambda_2 = 0.01$, the correction of 10% is in line with the correction found for the 2 other benchmark points while the corrections for $\lambda_2 = 1, 2$ are sensibly smaller. Nonetheless, we warn the reader again that a large value of β_{λ_L} is sensitive to large scale variations. Independently of the scale choice, a common feature is that $\lambda_2 = 0.01$ gives the smallest correction often approaching the tree-level improved $\alpha(M_Z^2)$ approximation.

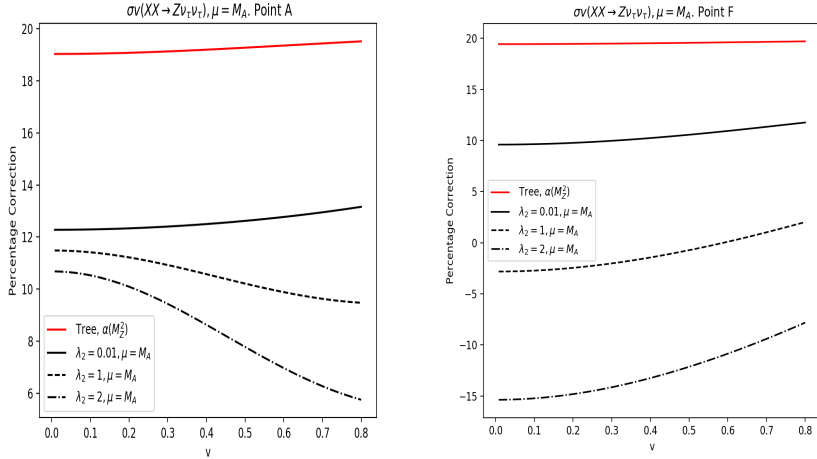


Figure 6: The relative corrections for $\sigma v(XX \rightarrow Z\nu_\tau\bar{\nu}_\tau)$ with $\mu = M_A$ for the benchmark Point A (left panel) and Point F (right panel).

5 $XX \rightarrow Zf\bar{f}$ and $XX \rightarrow Wf\bar{f}'$: one-loop results

We already saw in our study of the tree-level cross-sections in section 2 that the flavour dependence of $\sigma(XX \rightarrow Wf\bar{f}')$ is, to an excellent accuracy, contained in and represented by the flavour dependence of $\Gamma(W \rightarrow f\bar{f}')$. We also learnt that the velocity dependence of the neutral and charged channels cancels out in the ratio of the cross-sections $\sigma(XX \rightarrow Wf\bar{f}')/\sigma(XX \rightarrow Z\nu\bar{\nu})$ for velocities up to $v = 0.5$. Above these velocities, the WW channel starts experiencing the onset of the WW threshold while the ZZ is still not experiencing the ZZ threshold. The underlying global $SU(2)$ symmetry would also suggest that, particularly below $v < 0.5$, the λ_L dependence of $\sigma(XX \rightarrow Wf\bar{f}')/\sigma(XX \rightarrow Z\nu\bar{\nu})$ cancels out. To wit, we find that the λ_L dependence for $XX \rightarrow W\nu_\tau\bar{\nu}_\tau$ for point G and velocity $v = 0.4$ writes as

$$\begin{aligned} \sigma_{XX \rightarrow W\nu_\tau\bar{\nu}_\tau, G}^0(v = 0.4) &= 0.086 + 1.960\lambda_L + 11.343\lambda_L^2 \simeq 0.086 (1 + 23\lambda_L + 133\lambda_L^2) \\ &\simeq 6.585 \sigma_{XX \rightarrow Z\nu\bar{\nu}, G}^0(v = 0.4). \end{aligned} \quad (5.1)$$

The latter very good approximation means, especially for the very small values of λ_L we are permitted, that the μ dependence, Equation 4.2, is within machine precision and fitting procedure, identical for ZZ^* and WW^* . Since these two channels carry almost the same relative λ_L dependence and that $\lambda_L \ll 1$, the scale dependence for the normalised cross-sections is confirmed to be almost the same.

A small expected departure above $v > 0.5$ is confirmed numerically. The flavour independence of $\sigma(XX \rightarrow Wf\bar{f}')/\Gamma(W \rightarrow f\bar{f}')$ continues to hold true at one-loop. The latter stems from the fact that the electroweak radiative corrections (relative to the tree-level) of $\Gamma(W \rightarrow f\bar{f}')$ are known to be the same for all flavours [59], therefore $R_{Wf\bar{f}'}^{XX} = 1$ at one-loop also. We also verify all these properties by a direct full one-loop computation to the different channels. First of all, we confirm that the relative electroweak correction to the annihilation into $Wl\bar{l}'$ is, within the per-mille level, the same as that of the annihilation into $Wq\bar{q}'$, we therefore only show the leptonic (charged) final state, $W\tau\bar{\nu}_\tau$.

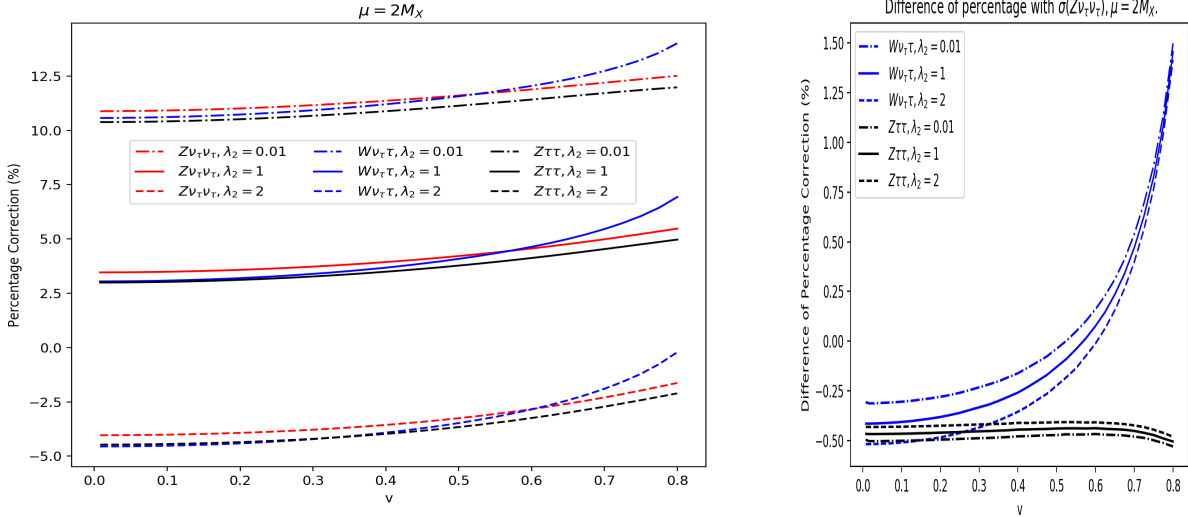


Figure 7: Point G. The relative correction, $d\sigma(Vf\bar{f}')/\sigma^0(Vf\bar{f}')$, $V = W, Z$ in % as a function of the relative velocity for $XX \rightarrow Z\tau^+\tau^-$, $Z\nu_\tau\bar{\nu}_\tau$, $W\tau\bar{\nu}_\tau$ for $\mu = 2M_X$ and $\lambda_2 = 0.01, 1, 2$. The right panel shows the difference $d\sigma(Vf\bar{f}')/\sigma(Vf\bar{f}') - d\sigma(Z\nu\bar{\nu})/\sigma(Z\nu\bar{\nu})$.

As Figure 7 for $\mu = 2M_X$ in the benchmark point G shows, the behaviour of all the annihilation channels follow $XX \rightarrow Z\nu_\tau\bar{\nu}_\tau$. The λ_2 dependence is indeed represented by the channel we discussed in detail in the previous section. The -0.5% difference between the $(Z)\tau\bar{\tau}$ and $(Z)\nu_\tau\bar{\nu}_\tau$ is indeed due mostly to the one-loop relative correction between the Z decay width into $\tau\bar{\tau}$ and $\nu_\tau\bar{\nu}_\tau$ (-0.9%) with a smaller contribution from the τ Yukawa mass (h exchange for example) as identified in Figure 2. The deviation observed in $W\tau\bar{\nu}_\tau$ increases for larger v (as expected from the tree-level comparison of these two channels). Nonetheless, the difference between the relative corrections remains below 1.5% (below 0.5% for $v < 0.5$). To an excellent approximation, the relative one-loop corrections, $d\sigma$, between the different channels, represent the difference between the one-loop electroweak corrections to the corresponding partial widths, $d\Gamma$,

$$\frac{d\sigma(XX \rightarrow Zf\bar{f}')v}{\sigma(XX \rightarrow Zf\bar{f}')v} - \frac{d\sigma(XX \rightarrow Z\nu\bar{\nu})v}{\sigma(XX \rightarrow Z\nu\bar{\nu})v} \simeq \frac{d\Gamma(Z \rightarrow f\bar{f}')}{\Gamma(Z \rightarrow f\bar{f}')} - \frac{d\Gamma(Z \rightarrow \nu\bar{\nu})}{\Gamma(Z \rightarrow \nu\bar{\nu})} \quad (5.2)$$

The mass effect is obviously more important for the b -quark final state channel, as we already saw at tree-level (Figure 2). In the radiative corrections to $\sigma v(XX \rightarrow Zb\bar{b})$, there is about a -6% difference with the $Z\nu\bar{\nu}$ channel, see Figure 8. Almost half of this correction is due to the difference in the relative electroweak correction between the partial width $Z \rightarrow b\bar{b}$ and $Z \rightarrow \nu\bar{\nu}$.

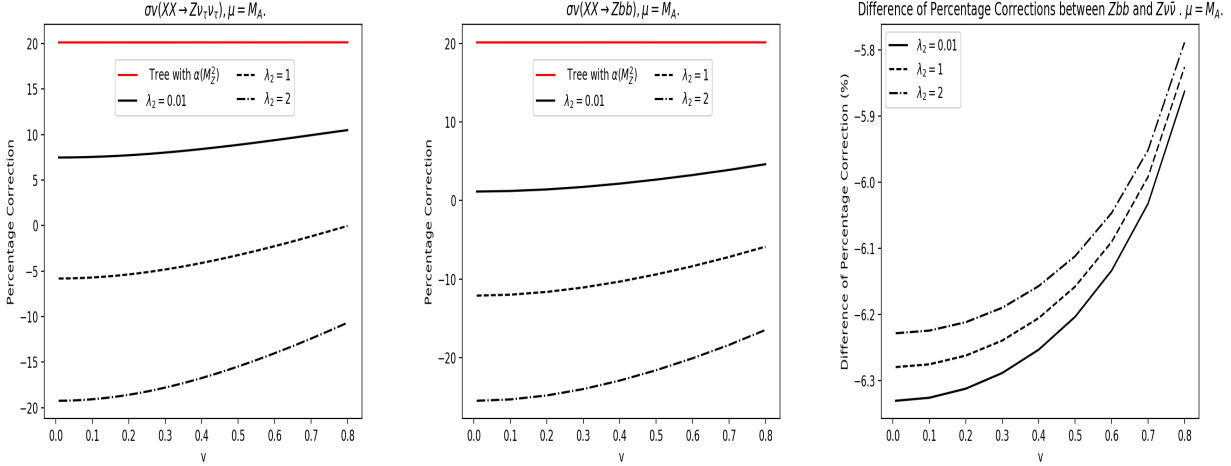


Figure 8: Point G. Percentage corrections for $\mu = M_A$ for the $Z\nu_\tau\bar{\nu}_\tau$ and $Zb\bar{b}$ final states. The latter are about 6% lower than the neutrino case for all values of v and λ_2 .

6 Intermediate Summary

Let us take stock.

- An important feature common to all three benchmarks is that whatever the values of the renormalisation scale μ and of the parameter λ_2 are, $XX \rightarrow Z\nu\bar{\nu}$ encapsulates practically all of the radiative corrections contained not only in the neutral channels $XX \rightarrow Zf\bar{f}$ but also in the charged channels $XX \rightarrow Wf\bar{f}'$, in the sense that the normalised one-loop corrections are, to a high degree of accuracy, equal for all channels for the same choice of λ_2 and the renormalisation scale μ

$$\frac{\delta\sigma(XX \rightarrow Z\nu\bar{\nu})}{\sigma(XX \rightarrow Z\nu\bar{\nu})}\Big|_{\mu,\lambda_2} \sim \frac{\delta\sigma(XX \rightarrow Vf\bar{f}')}{\sigma(XX \rightarrow Vf\bar{f}')}\Big|_{\mu,\lambda_2} \quad V = W, Z \quad (6.1)$$

- Equation 6.1 is valid at all v (in the range of interest for the relic density) for $\sigma(XX \rightarrow Zf\bar{f})$. There is a slight v dependence for $\sigma(XX \rightarrow Wf\bar{f}')$ when compared to $\sigma(XX \rightarrow Vf\bar{f})$. This difference is small and does not exceed more than 1.5%.

-There is no flavour dependence for the charged channels. The flavour dependence in the neutral channel is largest for $Zb\bar{b}$ where the largest difference amounts to 6%, more than half of this difference is accounted for by a correction given by $\Gamma(Z \rightarrow f\bar{f})_{1\text{-loopEW}}/\Gamma(Z \rightarrow f\bar{f})_{\text{tree}}$. We expect these small flavour effects to be diluted when we consider the correction to the relic density, considering that the ZZ channel accounts for about 10% to the relic density and that the $b\bar{b}$ channel is 15% of the whole ZZ .

- As expected, the scale dependence is largest for point A which has the largest $\tilde{\beta}_{\lambda_L}$. Our conjecture (based nonetheless on the study of the scales involved in the loop functions) seems to be a very good one. The appropriate scale is $\max(2M_X, M_A)$. In particular, we find that for $\lambda_2 = 0.01$, all 3 benchmark points give very similar corrections of about 10% – 12%. For this choice of scale, points F and G (which have small $\tilde{\beta}_{\lambda_L}$) give very similar corrections for $\lambda_2 = 1$ (–5%), 2 (–20%) while for point A, the corresponding corrections are v dependent with values for $v \sim 0$ similar for all λ_2 . We observe that in our study of $XX \rightarrow Wf\bar{f}'$ (P60) in

the co-annihilation region [50], where an on-shell renormalisation for λ_L was possible, the electroweak correction for $\lambda_2 = 0.01, 1, 2$ were *quantitatively* very similar to the results we obtain here, especially for the benchmark points F and G. This validates further our conjecture about the choice of scale. For the calculation of the relic density, we consider that the appropriate scale is $\max(\mu = 2M_X, M_A)$ and that theoretical uncertainty can be estimated by the difference within the range $(2M_X, M_A)$.

7 Effect on the relic density

	tree	$\alpha(M_Z^2)$	$\lambda_2 = 0.01$	$\lambda_2 = 1$	$\lambda_2 = 2$
Point G (I)	0.121	0.101 (-16.53%)			
Full, $\mu = M_X$			0.093 (-23.43%)	0.076 (-36.73%)	0.065 (-46.11%)
Full, $\mu = 2M_X$			0.109 (-9.53%)	0.117 (-3.47%)	0.125 (3.57%)
Full, $\mu = M_A$			0.112 (-7.27%)	0.126 (3.94%)	0.143 (18.51%)
Simplified, $\mu = M_X$			0.093 (-23.48%)	0.076 (-36.76%)	0.065 (-46.12%)
Simplified, $\mu = 2M_X$			0.109 (-9.60%)	0.117 (-3.55%)	0.125 (3.47%)
Simplified, $\mu = M_A$			0.112 (-7.35%)	0.126 (3.84%)	0.143 (18.37%)
Point A (B)	0.156	0.130 (-16.67%)			
Simplified, $\mu = M_X$			0.092 (-41.35%)	0.063 (-59.57%)	0.048 (-69.12%)
Simplified, $\mu = 2M_X$			0.125 (-19.59%)	0.112 (-28.28%)	0.101 (-35.31%)
Simplified, $\mu = M_A$			0.140 (-10.16%)	0.144 (-7.91%)	0.147 (-5.52%)
Point F (H)	0.119	0.099 (-16.81%)			
Simplified, $\mu = M_X$			0.098 (-17.92%)	0.089 (-25.23%)	0.082 (-31.38%)
Simplified, $\mu = 2M_X$			0.109 (-8.15%)	0.123 (3.62%)	0.142 (19.17%)
Simplified, $\mu = M_A$			0.108 (-8.82%)	0.120 (1.21%)	0.136 (13.94%)

Table 2: The relic density for points G, A and F at tree-level and after including the one-loop corrections. The percentage changes are given in parenthesis. The percentage correction corresponding to the use of $\alpha(M_Z^2)$ at tree-level is also indicated. The full corrections for point G differ from the simplified one-loop in that the full one-loop $Zb\bar{b}$ final state is fully taken into account while in the simplified version all fermion final states are rescaled from the full one-loop in the $Z\nu\bar{\nu}$ cross-section through the added one-loop flavour correction, $\Gamma_{Z\rightarrow f\bar{f}}/\Gamma_{Z\rightarrow\nu\bar{\nu}}$, where the partial widths are computed at one-loop, see text for details.

We just learnt that the v dependence of the cross-sections, that contributes to the relic density calculation, is rather smooth. Moreover, the μ (scale) dependence is sensibly the same in all channels (neutral and charged). We therefore expect the μ dependence of the relic density to follow that of the cross-section $\sigma(XX \rightarrow Z\nu\bar{\nu})$, since $\Omega h^2 \sim 1/\langle\sigma v\rangle$ ($\langle\sigma v\rangle$ is the total thermodynamically averaged cross-section). The difference between the values of the relic density for $\mu = M_X$ and $\mu = 2M_X$ follows this trend as shown in Table 2 of the relic densities obtained after passing all our tree and one-loop v dependent cross-sections to micrOMEGAs. The table shows (as expected) large corrections for the inappropriate choice $\mu = M_X$, particularly for point A. We derive the relic density by taking into account the Yukawa couplings of the b -quarks (full calculation) beyond the effect of the flavour

dependence contained in the partial decay $\Gamma_{Z \rightarrow b\bar{b}}$, see 5.2, that allows a nice factorisation of the total cross-section in terms of $\sigma(XX \rightarrow Z\nu\bar{\nu})$, which we call *simplified*. The difference between the full and simplified implementations is very small since the overall contribution of the $Zb\bar{b}$ final state to the total annihilation cross-section is small. An important feature seen for all scales and benchmark points is that the impact of λ_2 is large, this parameter is not taken into account when tree-level analyses are conducted.

The appropriate scale is $\max(\mu = 2M_X, M_A)$. For $\lambda_2 = 0.01$, the 3 benchmark points give very similar results with small corrections contained in the range -7% to -10% . These corrections are smaller than those found through the naive use of a running α at scale M_Z^2 . Even for these scales, the λ_2 dependence is not negligible at all. To give a quantitative estimate of the theory uncertainty that a tree-level evaluation of the relic density should incorporate, one needs to look at the one-loop results by varying both μ and λ_2 . For instance, take the benchmark point F (very similar results are obtained for point G) which has a small $\tilde{\beta}_{\lambda_L}$. While at tree-level, $\Omega h^2 = 0.119$ (obtained with $\alpha(0)$), the theory uncertainty now is $0.108 < \Omega h^2 < 0.142$ ($\Omega h^2 = 0.119_{-8.8\%}^{+19.2\%}$), this is more than the uncertainty of $\pm 10\%$ applied routinely in some analyses. Note that the uncertainty/error is much larger if based on the usage of $\alpha(M_Z^2)$ which is the default value of `micrOMEGAS`. For point A, where $\tilde{\beta}_{\lambda_L}$ is larger, the tree-level result is turned into the range $\Omega h^2 = 0.156_{-35.3\%}^{-5.5\%}$ with the conclusion that a value of 0.156 that could be dismissed on the basis of the present experimental constraint on the relic density can in fact be easily brought in line with the measured value if loop corrections were taken into account.

8 Conclusions

This is the first time a calculation of $2 \rightarrow 3$ processes for the annihilation of DM has been performed at the one-loop level and the results of the corrected cross-sections turned into a prediction of the relic density. While this calculation is within the IDM, the tools at our disposal are now powerful enough to tackle such calculations for any model of DM provided a coherent renormalisation programme has been devised and implemented. In the particular case of the IDM, the reconstruction of the model parameters in order to fully define the model leaves two underlying parameters not fully determined in terms of physical parameters. One parameter, λ_2 , describes, at tree-level, the interaction solely within the dark sector of the IDM. It is therefore difficult to extract *directly* from observables involving SM particles. Yet, this parameter contributes significantly to dark matter annihilation processes such as those we studied here. This indirect one-loop effect could in principle be extracted from the precise measurement of the relic density, a situation akin to the extraction of the top mass from LEP observables provided all other parameters of the model, masses of the additional scalars and their coupling to the SM, λ_L . λ_L , in fact measures the strength of the coupling of the SM Higgs to the pair of DM, there is in fact a one-to-one mapping between Higgs decay to XX and λ_L , which suggests an extraction of λ_L from the partial width of the Higgs into XX . While difficult in general, it is impossible when this Higgs decay is closed. The allowed parameter space for the $2 \rightarrow 3$ processes we studied is when this Higgs decay is closed. In this case we suggested an $\overline{\text{MS}}$ scheme for λ_L . The $\overline{\text{MS}}$ introduces a scale dependence on the one-loop cross-sections. We showed that the scale dependence can be determined from the λ_L parametric dependence of the tree-level cross-section and the knowledge of the 1-loop β constant for λ_L , $\tilde{\beta}_{\lambda_L}$. Despite the fact that the experimentally allowed values of λ_L are small, the parametric dependence of the cross-sections on λ_L are large for all the benchmarks that we studied. Combined with not so small $\tilde{\beta}_{\lambda_L}$, the scale dependence can be very large if an *inappropriate* scale is chosen. Based on a few other analyses in the framework of the IDM [50] and also in supersymmetric scenarios [57, 58] regarding the issue of the choice of the optimal scale, we

suggest to restrict the choice of the scale to values around the maximal scale involved in the process. The present one-loop analysis is yet another warning to practitioners of the IDM and other BSM models in respect of the relic density of DM in these models. The one-loop analyses give an important quantitative estimate of the (often) large theoretical uncertainty that should be taken into account before allowing or dismissing scenarios based on a tree-level derivation of relic density. The latter for instance is not sensitive to the value of λ_2 . λ_2 should be taken into account along side the uncertainty from the scale variation. We find that the combined theoretical uncertainty is model-dependent and in many cases is much larger than the cursory (\pm)*symmetric* 10% theoretical uncertainty that is included in many analyses.

Acknowledgments

We thank Alexander Pukhov for several insightful discussions. HS is supported by the National Natural Science Foundation of China (Grant , No.12075043, No.11675033). He thanks the CPTGA and LAPTh for support during his visit to France in 2019 when this work was started. SB is grateful for the support received from IPPP, Durham, UK, where most of this work was performed. SB is also grateful to the support received from LAPTh during his visit, when this work started. NC is financially supported by IISc (Indian Institute of Science, Bangalore, India) through the C.V. Raman postdoctoral fellowship. NC also acknowledges the support received from DST, India, under grant number IFA19-PH237 (INSPIRE Faculty Award).

References

- [1] N. G. Deshpande and E. Ma, *Pattern of Symmetry Breaking with Two Higgs Doublets*, *Phys. Rev.* **D18** (1978) 2574.
- [2] R. Barbieri, L. J. Hall and V. S. Rychkov, *Improved naturalness with a heavy Higgs: An Alternative road to LHC physics*, *Phys. Rev.* **D74** (2006) 015007, [[hep-ph/0603188](#)].
- [3] T. Hambye and M. H. G. Tytgat, *Electroweak symmetry breaking induced by dark matter*, *Phys. Lett.* **B659** (2008) 651–655, [[0707.0633](#)].
- [4] L. Lopez Honorez, E. Nezri, J. F. Oliver and M. H. G. Tytgat, *The Inert Doublet Model: An Archetype for Dark Matter*, *JCAP* **0702** (2007) 028, [[hep-ph/0612275](#)].
- [5] Q.-H. Cao, E. Ma and G. Rajasekaran, *Observing the Dark Scalar Doublet and its Impact on the Standard-Model Higgs Boson at Colliders*, *Phys. Rev.* **D76** (2007) 095011, [[0708.2939](#)].
- [6] M. Gustafsson, E. Lundstrom, L. Bergstrom and J. Edsjo, *Significant Gamma Lines from Inert Higgs Dark Matter*, *Phys. Rev. Lett.* **99** (2007) 041301, [[astro-ph/0703512](#)].
- [7] P. Agrawal, E. M. Dolle and C. A. Krenke, *Signals of Inert Doublet Dark Matter in Neutrino Telescopes*, *Phys. Rev.* **D79** (2009) 015015, [[0811.1798](#)].
- [8] T. Hambye, F. S. Ling, L. Lopez Honorez and J. Rocher, *Scalar Multiplet Dark Matter*, *JHEP* **07** (2009) 090, [[0903.4010](#)].
- [9] E. Lundstrom, M. Gustafsson and J. Edsjo, *The Inert Doublet Model and LEP II Limits*, *Phys. Rev.* **D79** (2009) 035013, [[0810.3924](#)].
- [10] S. Andreas, M. H. G. Tytgat and Q. Swillens, *Neutrinos from Inert Doublet Dark Matter*, *JCAP* **0904** (2009) 004, [[0901.1750](#)].
- [11] C. Arina, F.-S. Ling and M. H. G. Tytgat, *IDM and iDM or The Inert Doublet Model and Inelastic Dark Matter*, *JCAP* **0910** (2009) 018, [[0907.0430](#)].
- [12] E. Dolle, X. Miao, S. Su and B. Thomas, *Dilepton Signals in the Inert Doublet Model*, *Phys. Rev.* **D81** (2010) 035003, [[0909.3094](#)].

- [13] E. Nezri, M. H. G. Tytgat and G. Vertongen, *$e+$ and anti- p from inert doublet model dark matter*, *JCAP* **0904** (2009) 014, [[0901.2556](#)].
- [14] X. Miao, S. Su and B. Thomas, *Trilepton Signals in the Inert Doublet Model*, *Phys. Rev.* **D82** (2010) 035009, [[1005.0090](#)].
- [15] J.-O. Gong, H. M. Lee and S. K. Kang, *Inflation and dark matter in two Higgs doublet models*, *JHEP* **04** (2012) 128, [[1202.0288](#)].
- [16] M. Gustafsson, S. Rydbeck, L. Lopez-Honorez and E. Lundstrom, *Status of the Inert Doublet Model and the Role of multileptons at the LHC*, *Phys. Rev.* **D86** (2012) 075019, [[1206.6316](#)].
- [17] B. Swiezewska and M. Krawczyk, *Diphoton rate in the inert doublet model with a 125 GeV Higgs boson*, *Phys. Rev.* **D88** (2013) 035019, [[1212.4100](#)].
- [18] A. Arhrib, R. Benbrik and N. Gaur, *$H \rightarrow \gamma\gamma$ in Inert Higgs Doublet Model*, *Phys. Rev.* **D85** (2012) 095021, [[1201.2644](#)].
- [19] L. Wang and X.-F. Han, *LHC diphoton Higgs signal and top quark forward-backward asymmetry in quasi-inert Higgs doublet model*, *JHEP* **05** (2012) 088, [[1203.4477](#)].
- [20] A. Goudelis, B. Herrmann and O. Stal, *Dark matter in the Inert Doublet Model after the discovery of a Higgs-like boson at the LHC*, *JHEP* **09** (2013) 106, [[1303.3010](#)].
- [21] A. Arhrib, Y.-L. S. Tsai, Q. Yuan and T.-C. Yuan, *An Updated Analysis of Inert Higgs Doublet Model in light of the Recent Results from LUX, PLANCK, AMS-02 and LHC*, *JCAP* **1406** (2014) 030, [[1310.0358](#)].
- [22] M. Krawczyk, D. Sokolowska, P. Swaczyna and B. Swiezewska, *Constraining Inert Dark Matter by $R_{\gamma\gamma}$ and WMAP data*, *JHEP* **09** (2013) 055, [[1305.6266](#)].
- [23] P. Osland, A. Pukhov, G. M. Pruna and M. Purmohammadi, *Phenomenology of charged scalars in the CP-Violating Inert-Doublet Model*, *JHEP* **04** (2013) 040, [[1302.3713](#)].
- [24] T. Abe and R. Sato, *Quantum corrections to the spin-independent cross section of the inert doublet dark matter*, *JHEP* **03** (2015) 109, [[1501.04161](#)].
- [25] N. Blinov, J. Kozaczuk, D. E. Morrissey and A. de la Puente, *Compressing the Inert Doublet Model*, *Phys. Rev.* **D93** (2016) 035020, [[1510.08069](#)].
- [26] M. A. Díaz, B. Koch and S. Urrutia-Quiroga, *Constraints to Dark Matter from Inert Higgs Doublet Model*, *Adv. High Energy Phys.* **2016** (2016) 8278375, [[1511.04429](#)].
- [27] A. Ilnicka, M. Krawczyk and T. Robens, *Inert Doublet Model in light of LHC Run I and astrophysical data*, *Phys. Rev.* **D93** (2016) 055026, [[1508.01671](#)].
- [28] G. Belanger, B. Dumont, A. Goudelis, B. Herrmann, S. Kraml and D. Sengupta, *Dilepton constraints in the Inert Doublet Model from Run1 of the LHC*, *Phys. Rev.* **D91** (2015) 115011, [[1503.07367](#)].
- [29] A. Carmona and M. Chala, *Composite Dark Sectors*, *JHEP* **06** (2015) 105, [[1504.00332](#)].
- [30] S. Kanemura, M. Kikuchi and K. Sakurai, *Testing the dark matter scenario in the inert doublet model by future precision measurements of the Higgs boson couplings*, *Phys. Rev.* **D94** (2016) 115011, [[1605.08520](#)].
- [31] F. S. Queiroz and C. E. Yaguna, *The CTA aims at the Inert Doublet Model*, *JCAP* **1602** (2016) 038, [[1511.05967](#)].
- [32] A. Belyaev, G. Cacciapaglia, I. P. Ivanov, F. Rojas-Abatte and M. Thomas, *Anatomy of the Inert Two Higgs Doublet Model in the light of the LHC and non-LHC Dark Matter Searches*, *Phys. Rev.* **D97** (2018) 035011, [[1612.00511](#)].
- [33] G. Arcadi, A. Djouadi and M. Raidal, *Dark Matter through the Higgs portal*, *Phys. Rept.* **842** (2020) 1–180, [[1903.03616](#)].

- [34] B. Eiteneuer, A. Goudelis and J. Heisig, *The inert doublet model in the light of Fermi-LAT gamma-ray data: a global fit analysis*, *Eur. Phys. J.* **C77** (2017) 624, [[1705.01458](#)].
- [35] A. Ilnicka, T. Robens and T. Stefaniak, *Constraining Extended Scalar Sectors at the LHC and beyond*, *Mod. Phys. Lett.* **A33** (2018) 1830007, [[1803.03594](#)].
- [36] J. Kalinowski, W. Kotlarski, T. Robens, D. Sokolowska and A. F. Zarnecki, *Benchmarking the Inert Doublet Model for e^+e^- colliders*, *JHEP* **12** (2018) 081, [[1809.07712](#)].
- [37] P. M. Ferreira and D. R. T. Jones, *Bounds on scalar masses in two Higgs doublet models*, *JHEP* **08** (2009) 069, [[0903.2856](#)].
- [38] P. M. Ferreira and B. Swiezewska, *One-loop contributions to neutral minima in the inert doublet model*, *JHEP* **04** (2016) 099, [[1511.02879](#)].
- [39] S. Kanemura, S. Kiyoura, Y. Okada, E. Senaha and C. P. Yuan, *New physics effect on the Higgs selfcoupling*, *Phys. Lett.* **B558** (2003) 157–164, [[hep-ph/0211308](#)].
- [40] E. Senaha, *Radiative Corrections to Triple Higgs Coupling and Electroweak Phase Transition: Beyond One-loop Analysis*, *Phys. Rev. D* **100** (2019) 055034, [[1811.00336](#)].
- [41] J. Braathen and S. Kanemura, *On two-loop corrections to the Higgs trilinear coupling in models with extended scalar sectors*, *Phys. Lett. B* **796** (2019) 38–46, [[1903.05417](#)].
- [42] A. Arhrib, R. Benbrik, J. El Falaki and A. Jueid, *Radiative corrections to the Triple Higgs Coupling in the Inert Higgs Doublet Model*, *JHEP* **12** (2015) 007, [[1507.03630](#)].
- [43] C. Garcia-Cely, M. Gustafsson and A. Ibarra, *Probing the Inert Doublet Dark Matter Model with Cherenkov Telescopes*, *JCAP* **1602** (2016) 043, [[1512.02801](#)].
- [44] S. Banerjee and N. Chakrabarty, *A revisit to scalar dark matter with radiative corrections*, *JHEP* **05** (2019) 150, [[1612.01973](#)].
- [45] R. Basu, S. Banerjee, M. Pandey and D. Majumdar, *Lower bounds on dark matter annihilation cross-sections by studying the fluctuations of 21-cm line with dark matter candidate in inert doublet model (IDM) with the combined effects of dark matter scattering and annihilation*, [2010.11007](#).
- [46] H. Abouabid, A. Arhrib, R. Benbrik, J. E. Falaki, B. Gong, W. Xie et al., *One-loop radiative corrections to $e^+e^- \rightarrow Zh^0/H^0A^0$ in the Inert Higgs Doublet Model*, [2009.03250](#).
- [47] J. Kalinowski, T. Robens, D. Sokolowska and A. F. Zarnecki, *IDM benchmarks for the LHC and future colliders*, [2012.14818](#).
- [48] S. Banerjee, F. Boudjema, N. Chakrabarty and H. Sun, *Relic density of dark matter in the inert doublet model beyond leading order: Renormalisation and Constraints for the low mass region*, .
- [49] S. Banerjee, F. Boudjema, N. Chakrabarty, G. Chalons and H. Sun, *Relic density of dark matter in the inert doublet model beyond leading order: The heavy mass case*, *Phys. Rev.* **D100** (2019) 095024, [[1906.11269](#)].
- [50] S. Banerjee, F. Boudjema, N. Chakrabarty and H. Sun, *Relic density of dark matter in the inert doublet model beyond leading order: Co-annihilation in the low mass region*, .
- [51] F. Boudjema, A. Semenov and D. Temes, *Self-annihilation of the neutralino dark matter into two photons or a photon and a photon in the minimal supersymmetric standard model*, *Physical Review D* **72** (Sep, 2005) .
- [52] N. Baro, F. Boudjema and A. Semenov, *Full one-loop corrections to the relic density in the MSSM: A Few examples*, *Phys. Lett.* **B660** (2008) 550–560, [[0710.1821](#)].
- [53] N. Baro, F. Boudjema and A. Semenov, *Automatised full one-loop renormalisation of the MSSM. I. The Higgs sector, the issue of $\tan(\beta)$ and gauge invariance*, *Phys. Rev.* **D78** (2008) 115003, [[0807.4668](#)].
- [54] N. Baro, F. Boudjema, G. Chalons and S. Hao, *Relic density at one-loop with gauge boson pair production*, *Phys. Rev.* **D81** (2010) 015005, [[0910.3293](#)].

- [55] F. Boudjema, G. Drieu La Rochelle and S. Kulkarni, *One-loop corrections, uncertainties and approximations in neutralino annihilations: Examples*, *Phys. Rev. D* **84** (2011) 116001, [[1108.4291](#)].
- [56] F. Boudjema, G. Drieu La Rochelle and A. Mariano, *Relic density calculations beyond tree-level, exact calculations versus effective couplings: the ZZ final state*, *Phys. Rev.* **D89** (2014) 115020, [[1403.7459](#)].
- [57] G. Bélanger, V. Bizouard, F. Boudjema and G. Chalons, *One-loop renormalization of the NMSSM in SloopS: The neutralino-chargino and sfermion sectors*, *Phys. Rev. D* **93** (2016) 115031, [[1602.05495](#)].
- [58] G. Bélanger, V. Bizouard, F. Boudjema and G. Chalons, *One-loop renormalization of the NMSSM in SloopS. II. The Higgs sector*, *Phys. Rev.* **D96** (2017) 015040, [[1705.02209](#)].
- [59] D. Bardin, S. Riemann and T. Riemann, *Electroweak One Loop Corrections to the Decay of the Charged Vector Boson*, *Z. Phys. C* **32** (1986) 121–125.